Check for updates

Exploring untapped potential of the molecular precursor approach to control fluorine-doping in mesostructured titania for acid catalysis

Fouad Elgayar, [iD] [a] Erwann Jeanneau,[b] Pascal Bargiela,[a] Adel Mesbah, [iD] [a] Nadine Essayem*[a] and Shashank Mishra [iD] *[a]

Employing molecular precursors with well-defined F/Ti ratios, this work presents a facile way to introduce fluorine inside the titania matrix in a controlled manner. A tunable library of new fluorinated Ti(IV) molecular precursors with F/Ti ratios varying in the range of 4.8–24 were synthesized, thoroughly characterized (single-crystal X-ray structures, IR, ^{1}H, ^{13}C and ^{19}F NMR, TGA), and studied for their hydrolysis and condensation characteristics. Hydrolysis of these precursors led to mesostructured fluorinated titania nanoparticles, in which the doping amount was broadly governed by the F-content of the precursors (XRF and XPS studies). The introduction of fluorine species in the TiO_2 matrix significantly enhances the acid properties, particularly the Brønsted acidity of the resulting materials, as indicated by NH_3 adsorption calorimetry and pyridine adsorption FTIR studies. This is supported by activity and selectivity changes in two model reactions upon fluorination of TiO_2: i) isopropanol conversion in the gas phase leading to formation of propene at the expense of acetone and ii) dihydroxy acetone conversion in the aqueous phase with enhanced formation of pyruvaldehyde and parallel suppression of Lewis acid-catalyzed lactic acid as well as base-catalyzed sugar formation.

Introduction

Traditionally, fossil fuels have been the primary sources of energy for mankind. Driven by the depletion of fossil fuel resources and the environmental impact of their large-scale combustion, producing alternative energy, fuels, and chemicals from biomass, which is available in abundance in the form of lipids, starch, algae, and lignocellulose, has become an actively pursued research theme.[1] In particular, accessing alkane-based biofuels from biomass has received significant attention.[2] The route to long-chain hydrocarbons *via* decarboxylation of fatty acids or hydroxyalkylation of furan derivatives derived from lignocellulosic waste has great potential for breakthrough technologies.[3,4] Acid catalysts are fast emerging as catalysts of choice for such reactions and quite a few acid catalysts such as Nafion-type resins, acidified bi-functional Pt/MCM-41 or Pd/NbOPO$_4$/SBA15 have been used in one-step synthesis of long-chain hydrocarbons from

furan derivatives.[5–7] Further development in the efficiencies of these catalysts in terms of their acidic properties and porosity is expected to revolutionize the field.[8]

Titania is an extraordinarily active catalyst for photo and acid–base catalysis.[9,10] It is cost-efficient, nontoxic, and chemically stable and unlike most other acid catalysts, shows remarkable water-tolerance properties. The latter properties are mandatory to minimize the poisoning or leaching of the catalyst's acid species in water. To boost further the Brønsted and Lewis acid character of titania, several strategies including doping it with low amounts of species capable of providing Lewis acid centers have been reported in the recent past.[10–12] In this context, the controlled incorporation of the most electronegative element, *i.e.* fluorine, is expected to enhance further the Brønsted and Lewis acid character of titania.[13–15] Indeed, metal fluorides have already been used as effective solid acid catalysts in various reactions such as the cracking of *n*-heptane or the hydroisomerisation of *n*-pentane.[16] Although fluorinated titania has been studied, usually with a small % of doping for photocatalytic application,[17,18] its potential in acid catalysis remains much less explored. The most common challenges in preparing these materials include i) the usually low-surface area of the metal-fluoride species and ii) the difficulty in controlling and reproducing the fluorine content and its homogeneous distribution. The latter stems from the fact that besides being incorporated in the titania lattice in the

[a] *Institut de Recherches sur l'Environnement et la Catalyse de Lyon (IRCELYON), CNRS, Université Claude Bernard Lyon 1, 69626, Villeurbanne, France.*
E-mail: nadine.essayem@ircelyon.univ-lyon1.fr,
shashank.mishra@ircelyon.univ-lyon1.fr
[b] *Centre de Diffractométrie Henri Longchambon, Université Claude Bernard Lyon 1, 5 rue de La Doua, 69100 Villeurbanne, France*

6744 | *Catal. Sci. Technol.*, 2025, **15**, 6744–6756

This journal is © The Royal Society of Chemistry 2025

form of $TiO_{2-x}F_y$, some fluoride can also be chemisorbed on the surface, with the exact mode and content of fluorination depending strongly on the synthetic methods and reaction conditions including the pH of the medium and the concentration of the fluorinating reagent.[18] The toxic nature of most fluorinating reagents, including the commonly used HF, is also a significant problem.

Most of the above challenges can potentially be addressed by the molecular precursor approach.[19] In the recent past, we reported the synthesis of metal oxides with controlled fluoride content by using designed fluorinated molecular precursors in CVD.[20] The sol–gel approach, on the other hand, is expected to result in oxides with controlled porosity and high surface area.[21] Metal aminoalkoxide derivatives are very attractive as sol–gel precursors for metal oxide nanomaterials because of their favorable hydrolysis and condensation characteristics as well as transformation into oxide at relatively low temperature.[22–26] In this work, we demonstrate that using designed titanium molecular precursors with well-defined F/Ti ratios in the sol–gel process leads to nanometric titania with i) a high amount of fluorine incorporated in a homogeneous, controlled and reproducible manner and ii) a high surface area with mesoporosity. As a result, better control over its acidic properties and accessibility of active sites are achieved. This strategy also allowed us to avoid the use of highly corrosive HF, which is usually employed as a fluorinating reagent. Rather, we used home-made fluorinated amino alcohols to synthesize new well-defined heteroleptic Ti(IV) aminoalkoxides with varying F/Ti ratios. These derivatives performed very well as precursors in the sol–gel process and upon hydrolysis afforded mesoporous TiO_2 with controlled fluorine content and high surface area. The acidic properties of a representative F–TiO_2 catalyst were measured using pyridine adsorption and NH_3 adsorption calorimetry studies and its catalytic performances were investigated in two model reactions: isopropanol conversion in the gas phase and dihydroxy acetone conversion in the aqueous phase. To the best of our knowledge, such an approach has never been reported to obtain fluorinated heterogeneous catalysts, in particular fluorinated titania, and is expected to offer real potential for innovation in the field of heterogeneous acid catalysis.
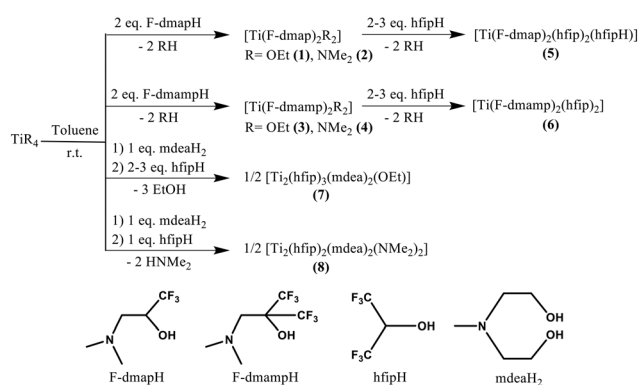
Results and discussion

(a) Synthesis of a tunable library of new Ti(IV) aminofluoroalkoxides

The first objective of this work was to develop a library of new Ti(IV) precursors with different intrinsic fluorine contents to control fluorine doping in mesostructured titania for acid catalysis. To achieve this goal, we employed a series of aminoalcohols for the synthesis of new heteroleptic titanium(IV) aminoalkoxides with different F : Ti ratios. The titanium reagent Ti(R)$_4$ (R = OEt or NMe$_2$) reacted with two equivalents of homemade potentially bidentate fluorinated N,N-dimethylaminopropanols [HOC(R^1)(R^2)CH$_2$N(CH$_3$)$_2$] [R^1 = H, R^2 = CF$_3$ (F-dmapH); R^1 = R^2 = CF$_3$ (F-dmampH)] in n-hexane or

toluene to give new titanium(IV) fluoroaminoalkoxides [Ti(R)$_2$(F-dmap)$_2$] [R = OEt (1), NMe$_2$ (2)] and [Ti(R)$_2$(F-dmamp)$_2$] [R = OEt (3), NMe$_2$ (4)] as colorless or orange liquids or low-melting solids (Scheme 1). The OEt or NMe$_2$ groups in 1–4 can further be replaced with hexafluoroisopropanol [HOCH(CF$_3$)$_2$ (hfipH)] to afford [Ti(F-dmap)$_2$(hfip)$_2$(hfipH)] (5) and [Ti(F-dmamp)$_2$(hfip)$_2$] (6) with enhanced fluorine content. We also employed nonfluorinated and potentially tridentate N-methyldiethanolamine [(HOCH$_2$CH$_2$)$_2$NMe] (mdeaH$_2$) along with hfipH to synthesize [Ti$_2$(mdea)$_2$(hfip)$_3$(OEt)] (7) and [Ti$_2$(mdea)$_2$(hfip)$_2$(NMe$_2$)$_2$] (8) in very good yields (Scheme 1). We have shown previously the excellent sol–gel properties of the mdeaH$_2$ ligand in obtaining catalytically superior nanomaterials.[22,24] We then exploited controlled partial hydrolysis as a strategy to condense the above precursors to well-defined oligomeric species with different F : Ti ratios. Thus, the F-dmap precursors 1 and 2 as well as the F-dmamp precursors 3 and 4, upon partial hydrolysis, afforded well-crystalline dimeric species [Ti$_2$O$_2$(F-dmap)$_4$] (9) and [Ti$_2$O$_2$(F-dmamp)$_4$] (10), respectively, in good yields. On the other hand, the *in situ* hydrolysis during the reaction of Ti(OEt)$_4$ with mdeaH$_2$ and hfipH in n-pentane afforded [Ti$_5$O$_3$(mdea)$_5$(hfip)$_4$] (11). These air-sensitive derivatives are liquids/low-melting solids (1–4) or crystalline solids (5–11) and are soluble in common organic solvents.

i) Single crystal X-ray crystallographic characterization. Suitable crystals of solid fluorinated precursors 5–11 were obtained and studied by single crystal X-ray diffraction analysis for their solid-state structures. Some crystallographic and refinement data as well as selected bond length and angle values for these complexes are provided in the SI as Tables S1–S8. The monomeric complex [Ti(η^2-F-dmap)(η^1-F-dmap)(η^1-hfip)$_2$(η^1-hfipH)] (5) crystallizes in the monoclinic space group $P2_1/n$, in which one F-dmap ligand is coordinated to the Ti^{IV} center in an N,O-chelating bidentate manner (Fig. 1a), whereas the other one is bonded in a monodentate fashion through its oxygen. Three terminal hexafluoroisopropanol ligands (two in deprotonated and one in protonated form) in the meridional position then complete the six-coordination around the titanium center, with the environment being O$_5$N (Fig. 1a). The

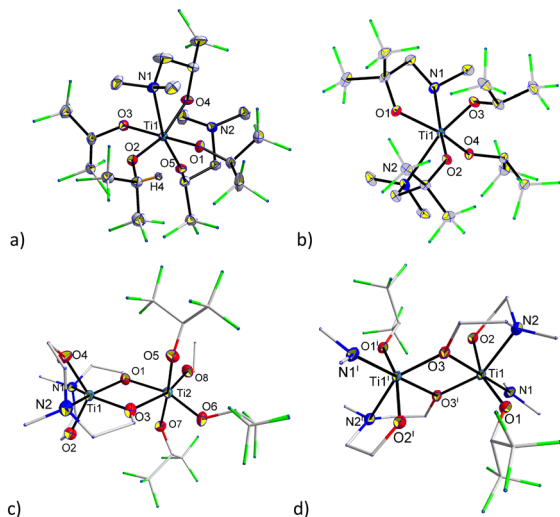Scheme 1 Synthesis of new heteroleptic Ti(IV) aminofluoroalkoxides 1–8.

Fig. 1 Molecular structures of (a) [Ti(F-dmap)$_2$(hfip)$_2$(hfipH)] (**5**), (b) [Ti(F-dmamp)$_2$(hfip)$_2$] (**6**), (c) [Ti$_2$(mdea)$_2$(hfip)$_3$(OEt)] (**7**) and (d) [Ti$_2$(mdea)$_2$(hfip)$_2$(NMe$_2$)$_2$] (**8**) with displacement ellipsoids drawn at the 50% probability level. H atoms are omitted for clarity.

Ti–O distance for the η^1-F-dmap ligand is significantly shorter (1.847 Å) than those involving η^2-F-dmap (1.957 Å) and the hfip ligands (1.912–1.934 Å). These Ti–O and Ti–N (2.344 Å) bond lengths are consistent with literature values.[22] The octahedral environment around the Ti center is considerably distorted as indicated by the *cis* O–Ti–O and O–Ti–N angles ranging from 76.13(7) to 106.97(7)°. The complex [Ti(η^2-F-dmamp)$_2$(η^1-hfip)$_2$] (**6**), which crystallizes in the orthorhombic space group *Pbca*, is also monomeric. Contrary to the previous complex, both fluorinated aminoalkoxide ligands here are coordinated to the Ti(ɪᴠ) center in an *N,O*-chelating bidentate manner, probably because the bite angle of the hexafluoro F-dmamp ligand in **6** (73.3–74.3°) is slightly less than that of the trifluoro F-dmap ligand in **5** (76.6°) (Fig. 1b). Two terminal hfip groups in the *cis*-position complete a distorted octahedral geometry around the metal center. The Ti–N and Ti–O bond lengths spread in the range of 2.357–2.385 and 1.849–1.890 Å, respectively, and are comparable with those of complex **5**. The dimeric structure of [Ti$_2$(μ-mdea)$_2$(hfip)$_3$(OEt)] (**7**) can formally be assumed as an association of [Ti(η^1-hfip)$_4$(η^1-OEt)] and [Ti(μ-mdea)$_2$] moieties bridged by one alkoxide arm of each bridging–chelating mdea ligand (Fig. 1c). All the hfip and OEt ligands are terminal and bonded to one titanium center, thus making the structure quite unsymmetrical. The two titanium centers are 6-coordinated with the MO$_6$ and MO$_4$N$_2$ environment, respectively. In contrast, the structure [Ti$_2$(mdea)$_2$(hfip)$_2$(NMe$_2$)$_2$] (**8**) is quite symmetric with each titanium bearing one bridging mdea, one terminal hfip and one terminal NMe$_2$ ligand to achieve a six-coordinated TiO$_4$N$_2$ coordination sphere (Fig. 1d). The bond lengths and angles are quite comparable in **7** and **8**. The terminal ethoxy group is the most strongly bound [Ti–O$_{OEt}$ 1.790(2) Å], followed by the aminoalkoxide [Ti–O$_{mdea}$ 1.821(2)–1.890(1) Å] and hfip [Ti–O$_{hfip}$ 1.915(2)–1.939(2) Å], while the bridging Ti–O$_{mdea}$ interactions are, unsurprisingly, weaker [1.973(2)–2.157(12) Å].
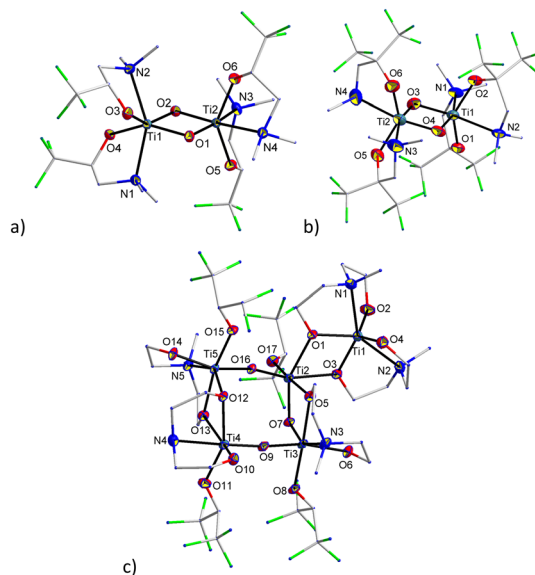

Fig. 2 Molecular structures of (a) [Ti$_2$(μ-O)$_2$(η^2-F-dmap)$_4$] (**9**), (b) [Ti$_2$(μ-O)$_2$(η^2-F-dmamp)$_4$] (**10**) and (c) [Ti$_5$(μ-O)$_3$(μ-mdea)$_5$(η^1-hfip)$_4$] (**11**) with displacement ellipsoids drawn at the 50% probability level. H atoms are omitted for clarity.

The Ti–N bond distances involving aminoalkoxide [Ti–N$_{mdea}$ 2.254(2)–2.279(2) Å] are longer than that involving the amide ligand [1.926(15) Å]. These Ti–O and Ti–N distances are consistent with those reported for related compounds such as [Ti$_2$(μ-mdea)(mdea)(μ-OEt)(OEt)$_3$][22] or [Ti(η^3-mdea)$_2$].[27]

Controlled hydrolysis of **1** or **2** and **3** or **4** in toluene afforded oxo-bridged dimeric complexes [Ti$_2$(μ-O)$_2$(η^2-dmap^F)$_4$] (**9**) and [Ti$_2$(μ-O)$_2$(η^2-dmamp^F)$_4$] (**10**) crystallizing in the monoclinic *P*2$_1$/*n* and orthorhombic *Pna*2$_1$ space groups, respectively (Fig. 2a and b). While **9** is non-solvated and has four molecules in the unit cell, complex **10**, depending on the synthetic/ crystallization conditions, crystallizes either with half or one solvated toluene and has a *Z* value equal to 16. At the molecular level, however, **9** and **10** are isostructural oxo-bridged dimeric complexes. Each titanium center of the Ti$_2$O$_2$ ring contains two fluorinated aminoalkoxide ligands coordinated in an *N,O*-chelating bidentate manner. Thus, each titanium is six-coordinated with a TiO$_4$N$_2$ coordination sphere. While **10** contains all four N atoms in the same plane of the Ti$_2$O$_2$ ring, there are only two of them in the same plane in **9**. The Ti–N distances (2.415–2.451 Å) for in-plane N-atoms (*i.e.* those *trans* to bridged oxo) are significantly larger than those for out-of-plane N-atoms (av. Ti–N = 2.268 Å). The bite angles of the F-dmap and F-dmamp ligands are in the range of 74.0–75.5° in **9** and **10**. The pentanuclear crystalline complex [Ti$_5$(μ-O)$_3$(μ-mdea)$_5$(η^1-hfip)$_4$] (**11**), obtained *via in situ* hydrolysis during the reaction of Ti(OEt)$_4$ with mdeaH$_2$ and hfipH, crystallizes in the monoclinic space group *P*2$_1$/*c*. The structure of **11** can formally be seen as an association of a planar tetranuclear cyclic structure {Ti$_4$(μ-O)$_3$(μ-mdea)$_3$(η^1-hfip)$_4$} with a {Ti(μ-mdea)$_2$} moiety (Fig. 2c). The structure is held together by bridging mdea and oxo groups while all the hfip ligands, which have a less

6746 | *Catal. Sci. Technol.*, 2025, **15**, 6744–6756

This journal is © The Royal Society of Chemistry 2025

Catalysis Science & Technology Paper

basic character due to the presence of highly electronegative fluorine atoms, are terminal. As observed in the previous structures **5–8**, the titanium centers have distorted octahedral geometries, with the environments being N_2O_4 (Ti1), NO_5 (Ti3, Ti4 and Ti5) or O_6 (Ti2). While the structure of the $\{Ti(\mu\text{-mdea})_2\}$ moiety is quite similar to that observed in the structure of **7**, that of $\{Ti_4(\mu\text{-O})_3(\mu\text{-mdea})_3(\eta^1\text{-hfip})_4\}$ is based on a cyclic Ti_4 core formed by two dinuclear $\{Ti_2(\mu\text{-mdea})_2(\eta^1\text{-hfip})_2\}$ bridged through two oxo ligands (Fig. 2c). Four titanium atoms and two bridging oxo ligands lie almost in a plane forming an unsymmetrical square with two *trans* Ti···Ti distances being 4.741 and 4.810 Å. The bridging oxo ligands are slightly shifted out from the square sides, as indicated by an angle of 166.1 and 168.1° at them. The T–O bond lengths vary from 1.830(2)–2.089(2) Å for mdea, 1.742(2)–1.917(2) Å for bridging oxo, and 1.912(2)–1.943(2) Å for hfip ligands, while the Ti–N bond lengths are in the range of 2.259(3)–2.359(2) Å.

ii) Spectroscopic characterization. The FT-IR and ^1H, ^{13}C and ^{19}F NMR spectra of the home-made fluorinated ligands F-dmapH and F-dmampH as well as their Ti(IV) complexes **1–11** are presented in Fig. S1–S13. The FT-IR spectra of **1–11** show the absence of a broad absorption band characteristic of the OH group in the 3250–3550 cm^{-1} region, indicating that the ligands were deprotonated. The presence of the fluorinated ligands was further confirmed by the strong bands in the regions of 2850–3000, 1300–1400 and 1000–1200 cm^{-1} due to $\nu(C(sp^3)\text{–H})$, $\nu(\text{–CF}_3)$ and $\nu(\text{O–C})$, respectively.[20] The appearance of new medium intensity bands at 400–600 cm^{-1} is due to Ti–O and Ti–N vibrations. The NMR spectra (^1H, ^{13}C and ^{19}F) for most compounds are unexceptional, which exhibit signals due to different ligands in the expected regions and intensity. For the monomeric complexes of the type $[Ti(R)_2(OR^F)_2]$ (R = OEt, NMe_2: OR^F = F-dmap or F-dmamp), five diastereoisomers are possible, among which three exist as pairs of enantiomers.[28] While the ^1H and ^{19}F NMR spectra of **2–4** are complex showing multiple peaks, those of **1** are quite simple, indicating the presence of a fluxional process at room temperature. Its ^1H NMR spectrum corresponds to the presence of a single species in solution with five peaks at δ 1.15 (t, 6H), 2.35 (s, 12H), 2.4–2.52 (dd, 4H), 4.37 (q, 4H) and 4.63 (m, 2H) due to OCH_2CH_3, NCH_3, NCH_2, OCH_2CH_3 and OCH_2, respectively. The ^{19}F NMR signal due to the CF_3 group of F-dmap appears at δ −79 ppm.

iii) Thermogravimetric studies. To understand the decomposition behavior and, therefore, to assess their suitability as precursors for F-doped TiO_2 materials, thermogravimetric analysis (TGA) of the fluorinated complexes **1–11** was performed (Fig. 3, S14 and Table S9). Besides providing an intrinsic source of fluorine for F-doped TiO_2 and improving the stability of the compounds, the fluorinated ligands are also expected to impart volatility in the precursors,[19] therefore, we were equally interested in assessing their potential as precursors for the chemical vapor deposition technique, even though the current article is essentially about using these precursors in the sol–gel process to obtain F-doped TiO_2. The precursors were sealed in aluminium pans and heated between
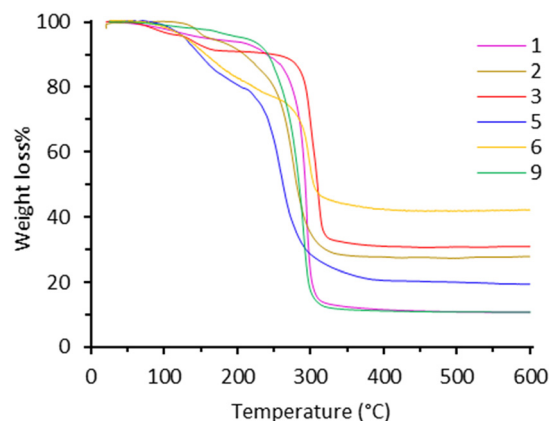

Fig. 3 TGA curves of the fluorinated Ti(IV) molecular precursors.

20 and 600 °C under an inert atmosphere. Some general observations and conclusions from TGA studies are: i) compounds **1** and **9** with the ligand F-dmap are the most volatile precursors showing a one-step weight loss with much less residual weight than expected for TiO_2 (Fig. 3, Table S9), ii) the bidentate fluorinated F-dmapH and F-dmampH ligands afford more volatility than the non-fluorinated mdeaH$_2$ ligand, iii) as compared to the NMe_2 ligand, the precursors with the OEt ligand show more defined and clean decomposition, and iv) all of these precursors are converted to F-doped TiO_2 between 300 and 350 °C as confirmed by XRD and XPS analyses of the residual powders.

(b) Fluorinated precursors to F-doped TiO_2 nanoparticles by sol–gel

The fluorinated precursors **1–11** were hydrolyzed with an excess of water at 100 °C in the presence of NH_4F to yield fluorine doped titania %F–TiO_2 nanoparticles, henceforth abbreviated as C-1 to C-11, respectively. The incorporation of fluorine in titania, particularly the surface-adsorbed species for which there is a competition between F^- and OH^- groups, is influenced by many factors including the pH and the concentration of the fluorinating reagent. The designed heteroleptic precursors **1–11**, which have a range of ligands with basic (amido, aminoalkoxo) and acidic (hfip) characteristics, present a large variation in the pH of the hydrolysis medium. Moreover, these ligands present different modes of bonding (mono or bidentate, terminal or bridging…) leading to different molecular structures (mono, di or pentanuclear), which potentially may influence the surface and acid properties of the resulting materials. For comparison, the un-doped TiO_2 obtained by the hydrolysis of $Ti(OEt)_4$ in the presence of NR_4Br is also presented.[29]

i) Structural, compositional and surface properties. The XRD patterns of all the F-doped TiO_2 samples match well with that of the undoped TiO_2, with all the peaks indexed well to the pure anatase phase (Fig. 4). However, as compared to undoped TiO_2, there is slight shifting in the peak positions for the F–TiO_2 samples, which indicates successful incorporation of the
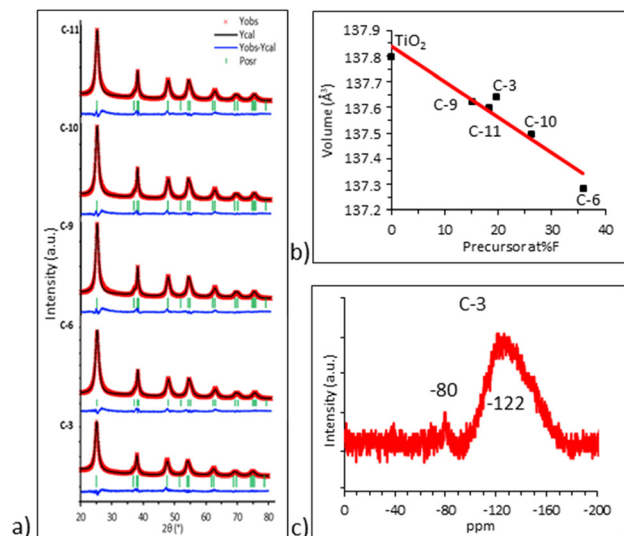
Fig. 4 (a) Rietveld-refined powder XRD patterns of selected F-doped TiO$_2$ catalysts C-3, C-6, C-9, C-10, and C-11, obtained by the hydrolysis of F-precursors **3**, **6**, **9**, **10** and **11**, respectively (referenced with PDF-02-021-1272), (b) the relationship between the TiO$_2$ cell volume in F–TiO$_2$ NPs and the atomic %F in the precursors, and (c) the ^{19}F MAS-NMR spectrum of C-3.

Fig. 5 XPS core-level F 1s (a) and Ti 2p (b) spectra of selected F-doped TiO$_2$ catalysts.

fluorine atoms in the TiO$_2$ matrix (Fig. S15). The Rietveld refinement of the powder XRD of some selected F-doped TiO$_2$ samples reveals no significant changes in the lattice parameters, except that the unit cell volume decreases slightly as a function of fluorine content in the precursors (Fig. 4b, Table S10).[30] The presence of fluorine in these catalysts is further confirmed by the ^{19}F MAS-NMR spectra of the selected samples. These spectra exhibit two ^{19}F MAS-NMR peaks in the range of δ 100 to −122 ppm, indicating different fluorine environments in TiO$_{2-x}$F$_y$ or on its surface (Fig. 4c and S16). Usually, the peak position is shifted to more negative values as the bonding mode changes from different bridging positions to the terminal one.[31] Subsequent fluorine environments and their corresponding ^{19}F NMR chemical shift values have been previously reported: Ti$^{IV}_2$–F (80–100 ppm), Ti$^{IV}_2\square$–F (~0 ppm), Ti$^{IV}_3$–F (−80 ppm), and TiF$_3$ (−150 ppm) (where $\square$ indicates cation vacancies).[32] A comparison of our ^{19}F MAS-NMR data with the above literature values suggests that the nature of the ligand sets and the structure of the precursors have a significant impact on the extent and the bonding types of fluorine inside the TiO$_2$ matrix and on its surface.

XPS analyses of F-doped titania catalysts gave further insights into the nature of F species together with their content and location (Fig. 5 and S17). The core-level F 1s XPS spectra exhibit two XPS peaks of varying intensity at ~684.5 and ~689 eV, which can be attributed to the surface-adsorbed F and lattice-bound TiO$_{2-x}$F$_y$ environment, respectively (Fig. 5a).[33] A similar binding energy difference of ~4 eV has been shown previously to differentiate between the surface and bulk fluorine species.[30] The different intensities of the two peaks in different samples can be linked to the different hydrolysis behavior of the precursors. As expected, the use of hfipH and
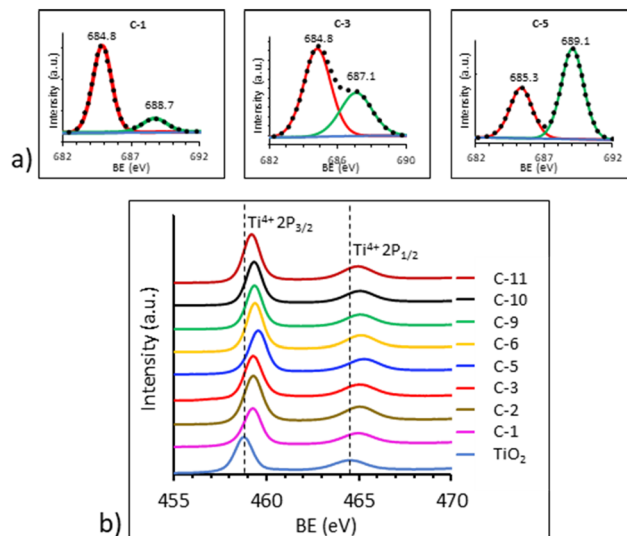
F-dmampH ligands with the highest numbers of fluorine atoms leads to high F-content inserted in the TiO$_2$ lattice. The Ti 2p spectra exhibit binding energies of 459.2–459.6 and 464.9–465.3 eV, corresponding to Ti 2p$_{3/2}$ and Ti 2p$_{1/2}$, respectively, which indicate the presence of Ti^{4+} species.[34] These values are slightly shifted in comparison with the undoped TiO$_2$ (Fig. 5b). The O 1s spectra show contributions from the Ti–O bond at ~530 eV with a slight shift due to the presence of fluorine, as well as O–H and C–O groups at ~531 and ~533 eV, respectively, originating from the organic residues of the precursor.[35] These organic residues of the precursor also contribute to the C 1s spectra which show peaks at 284–290 eV due to C–H, C–C, C–O and in some cases CF groups. The XPS quantitative analysis shows F-content varying from 1 to 5 at% in these catalysts. Furthermore, XRF analysis was also carried out to investigate their elemental analysis. Table 1 shows the atomic %F in the molecular precursors and the F-doped titania NPs by the XRF and XPS analyses. The different fluorine concentrations in the XPS and XRF studies can be attributed to the fact that XPS is more of a surface technique which analyzes the elements present only on the surface of the material. Fluorine insertion in the TiO$_2$ matrix is expected to cause O^{2-} vacancies leading to accumulation of more F$^-$ ions on the surface to balance the charge. This trend is not always followed among the F–TiO$_2$ catalysts here due to the different hydrolysis behavior of the precursors. By combining the results of the XRD, XPS, XRF and ^{19}F MAS-NMR studies, we can conclude that even though the hydrolysis of the above fluorinated molecular precursors follows a complex mechanism where not all fluorine atoms are inserted in the titania network (some remain as fluorinated organic residues chemisorbed on the surface of NPs), there is still a good relationship between fluorine contents in the molecular precursor and the final materials, thus giving atomic-level control and reproducibility of F% in TiO$_2$ nanocatalysts.

6748 | *Catal. Sci. Technol.*, 2025, **15**, 6744–6756

This journal is © The Royal Society of Chemistry 2025

Table 1 XRF and XPS fluorine atomic percentage quantification for F–TiO$_2$ catalysts

| Fluorinated molecular precursors | | | Fluorinated TiO$_2$ NPs | | |
| | | | | at %F | |
Compound	F/Ti ratio	at %F	Catalyst	XRF	XPS
[Ti(OEt)$_2$(F-dmap)$_2$] (**1**)	6	10.9	C-1	4.4	2.4
[Ti(NMe$_2$)$_2$(F-dmap)$_2$] (**2**)	6	10.5	C-2	6.6	5
[Ti(OEt)$_2$(F-dmamp)$_2$] (**3**)	12	19.7	C-3	16.6	4.9
[Ti(F-dmap)$_2$(hfip)$_2$(hfipH)] (**5**)	24	32.9	C-5	3.3	1.1
[Ti(F-dmamp)$_2$(hfip)$_2$] (**6**)	24	35.8	C-6	9	5
[Ti$_2$(O)$_2$(F-dmap)$_4$] (**9**)	6	15.0	C-9	9.8	4.8
[Ti$_2$(O)$_2$(F-dmamp)$_4$] (**10**)	12	26.1	C-10	5	4.2
[Ti$_5$O$_3$(mdea)$_5$(hfip)$_4$] (**11**)	4.8	18.2	C-11	4	3.2

Table 2 Textural and optical properties of undoped and F-doped TiO$_2$ NPs as deduced from N$_2$ adsorption–desorption isotherms and UV-vis optical absorption spectroscopy measurements

Sample[a]	S_{BET} (m^2 g^{-1})	S_{ext}[b] (m^2 g^{-1})	Ø meso[c] (nm)	Band gap (eV)
TiO$_2$	250	244	2–7	3.26
C-1	641	620	3–4	3.10
C-3	280	226	6–10	3.07
C-5	408	368	3–5	3.09
C-6	286	281	3–7	3.23
C-9	260	226	9–11	3.05
C-10	275	274	8–11	3.01
C-11	196	195	3–12	3.07

[a] Samples treated under vacuum for 24 h at 100 °C. [b] Deduced from t-plot results. [c] Deduced from the BJH method.

ii) Optical and textural properties. The optical band gaps of F-doped TiO$_2$ and undoped TiO$_2$ were measured using UV-vis optical absorption spectroscopy. As expected, F-insertion enhances the light absorption efficiency of the titania.[30,34] The direct band gap analysis as a function of K. M. [$(1 − R)^2$/$2R$] and photon energy (λ/eV) shows shifting of the absorption edge toward longer wavelengths (or lower band gap energy in eV) upon F-insertion (Fig. S18, Table 2). The N$_2$ adsorption/desorption isotherms of F–TiO$_2$ catalysts show typical type IV isotherms corresponding to mesoporous materials (Fig. 6). Although all precursors produce mesoporous F–TiO$_2$ with high surface area (Table 2), the types of ligands employed and their composition in the precursors have a clear influence on the surface area and pore-size distribution. Catalyst C-1 produced from precursor **1** presents a hysteresis loop which is different from others. The isotherm presents significant uptake at low relative pressure (0.4 and 0.7) and a hysteresis loop of type H2.[36] This can be attributed to facile hydrolysis and decomposition of **1** due to its rapid intramolecular rearrangement in solution (as indicated earlier by the ^{1}H NMR spectrum of this precursor). Indeed, fluxional molecules have previously been shown to act as efficient precursors in solution.[37] The nitrogen adsorption–desorption isotherms of C-9 and C-10 obtained from the hydrolysis of homoleptic [Ti$_2$(μ-O)$_2$(η^2-OR$_F$)$_4$] [OR$_F$ = F-dmap (**9**) and F-dmamp (**10**)] do not present important N$_2$ uptake at low relative pressure and are characterized by a hysteresis loop of type H3 at high relative pressure, >0.7.[38] This is consistent with the absence of micropores and the presence of large mesopores with diameters of 8–12 nm. Generally speaking, the heteroleptic precursors **1** and **5** with the F-dmap ligand produce the highest surface area of 641 and 408 m^2 g^{-1}, respectively. Other F-doped TiO$_2$ catalysts show either a comparable or slightly enhanced surface area compared to the 250 m^2 g^{-1} obtained for the undoped TiO$_2$ sample (Table 2).
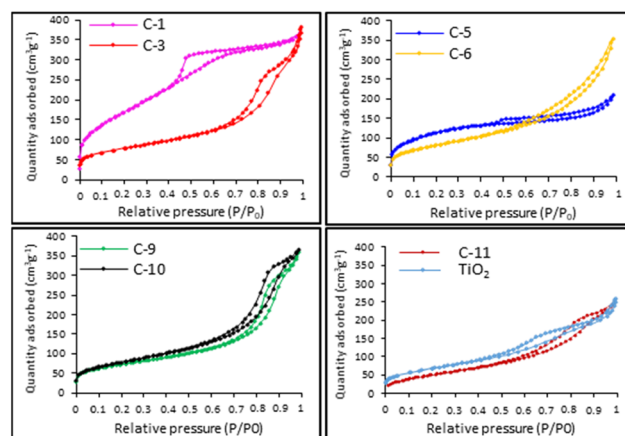

Fig. 6 N$_2$ adsorption/desorption isotherms of F-doped TiO$_2$ catalysts obtained from the hydrolysis of fluorinated Ti(IV) molecular precursors. The isotherm of the undoped TiO$_2$ NPs obtained from the hydrolysis of Ti(OEt)$_4$ is also shown for comparison.

This journal is © The Royal Society of Chemistry 2025

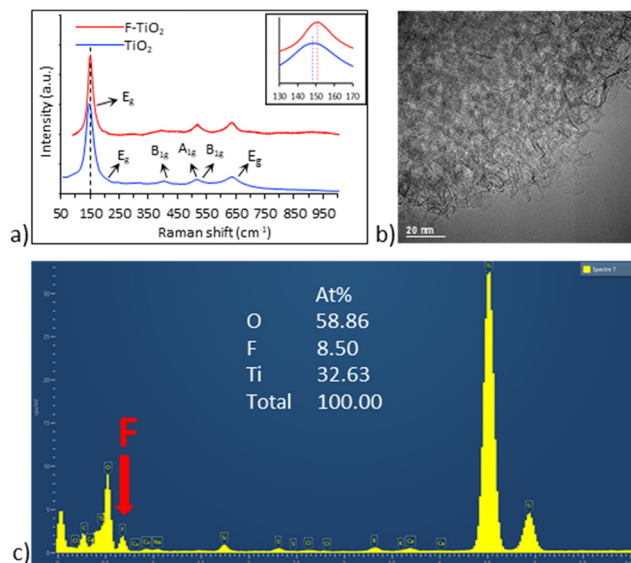*Catal. Sci. Technol.*, 2025, **15**, 6744–6756 | **6749**

Fig. 7 Additional characterization of the catalyst C-3 obtained from the hydrolysis of **3**: a) Raman spectrum, b) TEM image, and c) EDX spectrum.

Fig. 8 FTIR spectra of pyridine adsorption on (a) TiO_2 and (b) $F–TiO_2$ (C-3) catalysts (pyridine adsorption at RT for 30 min per desorption for 1 h at RT and 200 °C, each).

(c) Acidic and catalytic properties of a representative catalyst C-3 obtained from the hydrolysis of 3

Given its high F-content and mesoporous characteristics, the sample C-3 was chosen as a representative catalyst for studying its acid properties and catalytic activity. In addition to the characterization described in the previous section (XRD, XPS, XRF, ^{19}F NMR, N_2 adsorption/desorption isotherms), this catalyst was further characterized by Raman spectroscopy, TEM and EDX studies. Fig. 7a shows the Raman spectra of this F–TiO_2 (C-3) catalyst and the undoped TiO_2 NPs in the range of 100–1000 cm^{-1}. Both samples exhibit six characteristic Raman active modes $\Gamma = A_{1g} + 2B_{1g} + 3E_g$ for anatase TiO_2.[39] The peak at 147 cm^{-1} due to the E_g mode in TiO_2 is slightly shifted to 151 cm^{-1} for the F–TiO_2 catalyst. The nanometric form and F-content were confirmed by the TEM image and EDX analysis.

i) FTIR of pyridine-adsorption. To determine the nature of the acid sites present on the catalysts, FTIR experiments were performed using pyridine as a probe molecule. Fig. 8 shows the Py-FTIR spectra of the undoped and F-doped TiO_2 catalysts after saturation with pyridine vapor at ambient temperature and desorption under vacuum for 1 h at ambient temperature and 200 °C (to remove the physisorbed pyridine molecules). The FTIR spectra of undoped TiO_2 show strong bands at 1445 and 1607 cm^{-1} related to the vibrations of the pyridine molecule coordinated to the Lewis acid sites (Fig. 8a). Upon desorption, both bands showed a similar decrease in the intensity with the rise of the desorption temperature. On the other hand, the FTIR spectra of F-doped titania were characterized by the presence of additional bands at 1540 and 1638 cm^{-1} related to the pyridinium ion located on Brønsted acid sites (Fig. 8b). No change in the intensity of these two bands was observed with the rise of the desorption temperature. The band appearing at ~1490 cm^{-1}, which is characteristic of the presence of both
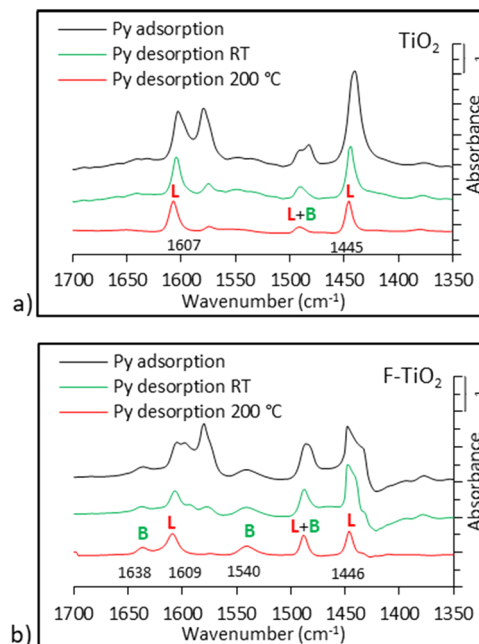
Brønsted and Lewis acidity,[40] is also more intense in the FTIR spectra of F-doped titania. Furthermore, no shifting of wavenumbers of the Lewis vibration at around 1446 cm^{-1} is observed after Py desorption at 200 °C. These results indicate that F-insertion in the titania catalysts does not increase the strength of the Lewis acid sites but generates the Brønsted acidity only.

ii) Microcalorimetry using NH_3 as a probe molecule. The undoped and F-doped TiO_2 catalysts were also analyzed by ammonia adsorption followed by microcalorimetry to determine the total acidity and the acid strength distribution.[12] Fig. 9a shows the isotherms of NH_3 adsorption for the undoped TiO_2 and F-doped TiO_2 catalysts, which were found to have 520 and 620 $\mu mol\ g^{-1}$ total number of acid sites, respectively. From these isotherms and the BET surface areas, acid site densities of 2.6 and 2.9 $\mu mol\ m^{-2}$ were calculated for the undoped TiO_2 and F-doped TiO_2 catalysts, respectively (Table 3). Moreover, the calorimetric curves of these catalysts present a pseudo plateau with a mean heat of NH_3 adsorption at half coverage of around 115 and 130 $kJ\ mol^{-1}\ NH_3$ for the F–TiO_2 and undoped TiO_2 catalysts, respectively, thus indicating a rather homogeneous acid site distribution in terms of acid sites' strength in these catalysts. In fact, a lower global acid strength is detected over F–TiO_2. This is consistent with the earlier Py-FTIR results on no Lewis acid strength enhancement but generation of Brønsted acidity only upon F-insertion.

iii) Acid catalytic properties. To study the catalytic activity of the above catalysts, we selected two model reactions: isopropanol conversion into propene/acetone in the gas phase and dihydroxy acetone conversion in the aqueous phase.[11,31,40]
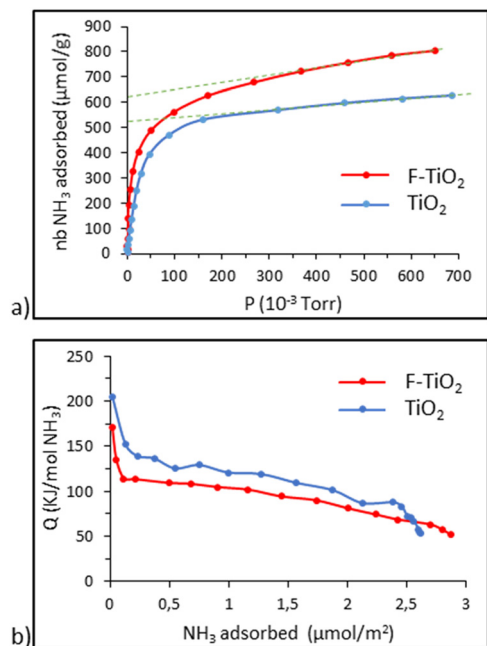
6750 | *Catal. Sci. Technol.*, 2025, **15**, 6744–6756

This journal is © The Royal Society of Chemistry 2025

Fig. 9 Calorimetry of NH$_3$ adsorption results over undoped and F-doped TiO$_2$ (C-3) catalysts: (a) detection of the number of acid sites and (b) enthalpy of NH$_3$ adsorption *versus* NH$_3$ uptake at 80 °C.

a) Isopropanol conversion reactions in the gas phase. Isopropanol catalytic dehydration over acidic catalysts to propene is a common reaction used to characterize the acid properties of catalysts. The acid-catalyzed pathway occurs through the carbenium ion mechanism leading mainly to propene formation,[41] whereas the base-catalyzed pathway leads to the formation of acetone *via* dehydrogenation of isopropanol into the corresponding carbanion (Scheme S1). Both F-doped and undoped TiO$_2$ catalysts led to the formation of propene as the main product, with a negligible amount of acetone being formed only by the latter. As compared to 8.5% conversion of isopropanol into propene by undoped TiO$_2$, the F-doped TiO$_2$ showed an up to 40% propene yield (Fig. 10a), both showing stable activity for 5 hours of continuous isopropanol flow. The turnover frequency (TOF) values were found to be 4.8 and 27.5 h^{-1} for the undoped TiO$_2$ and F–TiO$_2$ catalysts, respectively (Fig. 10b). Although undoped TiO$_2$ also presents a high number of acid sites and a stronger acidity, fluorinated titania showed a significantly high activity towards the dehydration of isopropanol into propene. These results are consistent with the presence of Brønsted acid sites on the surface of the fluorinated catalyst, which catalyze efficiently

isopropanol dehydration into propene at low temperature in contrast to the Lewis acid sites which require higher temperature. We also measured the catalytic performance of another catalyst (C-10) with a lower F-content but comparable surface area (5% F by XRF and 275 m^2 g^{-1} BET surface area) to determine the quantitative relationship between the fluorine content and catalytic performance. A comparison of these catalysts (C-3, C-10 and undoped TiO$_2$) shows that the increase in fluorine content enhances the catalytic performance significantly (Fig. S19). We also synthesized an F–TiO$_2$ sample using a traditional method by reacting titanium isopropoxide with trifluoroacetic acid as reported in the literature[17a] and tested its catalytic performance for isopropanol conversion. This F–TiO$_2$ sample, which has a lower F-content (2.04% F by EDX) and lower surface area (31 m^2 g^{-1}) as compared to the F–TiO$_2$ catalysts C-3 and C-10 (5–16.6% F by XRF and 275–280 m^2 g^{-1}) obtained *via* hydrolysis of our fluorinated molecular precursors, shows much inferior activity (Fig. S19). These results underline further the potential of the molecular precursor approach to obtain highly efficient acid catalysts.

b) DHA conversion reactions in the aqueous phase. To investigate further the acid–base catalytic potential of the fluorinated titania catalysts as well as to probe their water tolerance, we tested these catalysts for dihydroxyacetone (DHA) conversion in the aqueous phase (Fig. S20). The selectivity of this reaction depends not only on the Lewis/Brønsted acidity but also on the catalyst basicity: aqueous phase DHA conversion may produce not only pyruvaldehyde (PA) and lactic acid (LA) catalyzed by Brønsted/Lewis acid sites but also hexoses (C6) catalyzed by basic sites (Scheme S2). Fig. 11 shows the DHA conversion reactions catalyzed by TiO$_2$ and F–TiO$_2$ in water. As compared to the undoped titania, which showed more than 90% DHA conversion after 4 h of reaction, the F–TiO$_2$ catalyst was found to be less active (70% conversion under similar conditions) (Fig. 11a). The lower activity of fluorinated titania (TOF values of 9.2 h^{-1} and 4.1 h^{-1} for TiO$_2$ and F–TiO$_2$, respectively, based on the initial activity), despite having the highest total amount of acid sites, could be attributed to its surface hydrophobicity. The initial activity shows a preferable pyruvaldehyde (PA) production over F–TiO$_2$ in contrast to the LA formation found over undoped TiO$_2$. For undoped TiO$_2$, the maximum yield achieved for PA was 10% C, which was completely converted to LA at the end of the reaction to give an 85% C yield for the latter (Fig. 11b). Upon F-insertion, the catalyst became more selective towards PA formation (23.5% yield) all along the reaction course and its further transformation into LA was slow. These results are

Table 3 Acidic properties of F–TiO$_2$ and undoped TiO$_2$ deduced from calorimetry of NH$_3$ adsorption and FTIR of pyridine adsorption

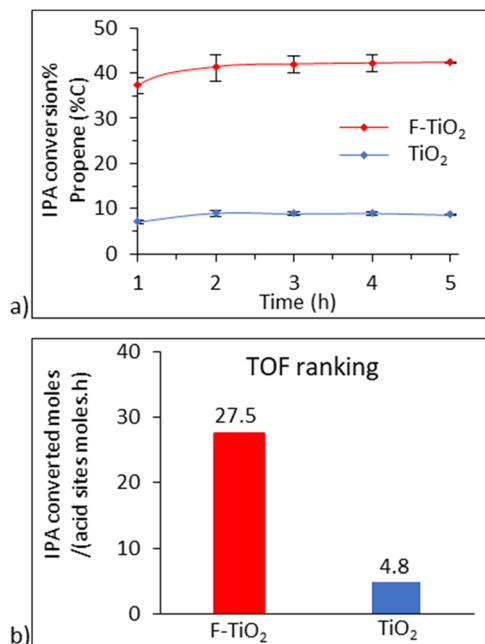| Sample	Total no. of acid sites (µmol g^{-1})	S_{BET} (m^2 g^{-1})	Acid site density (µmol m^{-2})	Py-ads Brønsted sites (%)	Py-ads Lewis sites (%)
TiO$_2$	520	250	2.6	0	100
F–TiO$_2$ (C-3)	620	280	2.9	44	56

Fig. 10 Isopropanol reactions performed over undoped TiO_2 and F-doped TiO_2 catalyst C-3: a) evolution of propene yields with time, and b) TOF values. Reaction conditions: 80 mg catalyst; total flow rate = 5 L h^{-1} (1% IPA in N_2); T = 200 °C; time on stream = 5 h.

consistent with the earlier conclusion that Brønsted acidity is more efficient than Lewis acidity in catalyzing DHA dehydration into PA,[42] while its further transformation into LA is promoted by Lewis acid sites only. To demonstrate further the enhanced
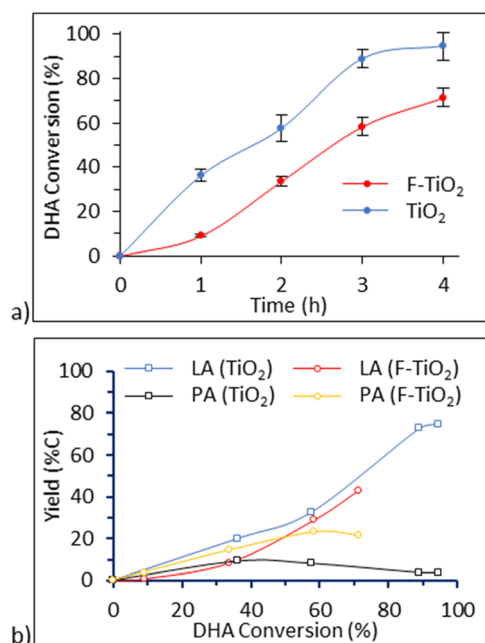

Fig. 11 a) DHA conversion catalyzed by undoped TiO_2 and F-doped TiO_2 catalyst C-3 and b) evolution of obtained products' yields (%C) as a function of the DHA conversion. Reaction conditions: 25 mg catalyst; DHA = 0.5 g L^{-1}; T = 120 °C; duration = 4 h; 6 bar argon.

hydrophobicity in F-doped TiO_2, we carried out contact angle measurements on catalyst C-3. The contact angle changed from 22.5° in TiO_2 to 48.5° for the fluorinated TiO_2 (Fig. S21), indicating the enhanced hydrophobicity of the F–TiO_2 sample. A similar finding has been reported previously in the literature.[43]

Conclusion

We reported here a novel molecular precursor approach to obtain fluorinated titania as a heterogeneous catalyst. For this, new fluorinated titanium(IV) complexes with different F/Ti atomic ratios were synthesized using homemade organic fluorinated ligands, fully characterized and employed as sol–gel precursors to obtain F-doped nanoparticles. The presence of fluorine enhances the acidity of titania catalysts by improving the proton donation capabilities, making fluorinated titania materials highly effective in Brønsted acid-catalyzed reactions. In comparison with undoped titania, a significant increase in the intrinsic Brønsted acid sites is observed for the F-doped titania which led to an enhancement of isopropanol conversion to propene in the gas phase as well as the catalyst stability. For DHA conversion in the aqueous phase, initial favored PA formation over F-TiO_2 accounts for its Brønsted activity. However, after 4 h, a high yield of lactic acid as the main product was observed for both undoped and F-doped TiO_2 catalysts, which could be correlated to the presence of water tolerant Lewis acid sites on them. However, lower performances were observed over fluorinated titania as compared to the undoped titania, most likely due to its surface hydrophobicity. The molecular precursor route reported here allows better control of the degree and form of fluorination of TiO_2 nanoparticles as well as precise tuning of surface properties, mesoporosity and acid properties of these catalysts, and is expected to open a new window for the controlled synthesis of heterogeneous acid catalysts.

Experimental section

All manipulations related to the synthesis of precursors and materials were carried out under argon using the Schlenk technique and a glove box. *N,N*-Dimethylamine (Sigma-Aldrich), 3,3,3-trifluoro-1,2-epoxypropane (ABCR GmbH), hexafluoroisobutene oxide (ABCR GmbH), and hexafluoro-isopropanol (Sigma-Aldrich) were purchased and used as received. [Ti(NMe$_2$)$_4$] and [Ti(OEt)$_4$] (Strem) were used after distillation under vacuum. Toluene, *n*-hexane, dichloromethane and ethanol used for the synthesis and crystallization of metal complexes were dried using MB SPS-800 or standard methods with appropriate desiccating reagents and distilled prior to their use. Two fluorinated amino-alcohol ligands namely 3,3,3-trifluoro-1-dimethylamino-2-propanol (F-dmapH) and 3,3,3-trifluoro-2-trifluoromethyl-1-dimethylamino-2-propanol (F-dmampH) were synthesized using literature methods.[20] The FT-IR spectra of the ligands and air-sensitive precursors **1–11** were recorded as Nujol mulls using a Bruker Vector 22 FT-IR spectrophotometer equipped with a DTGS detector. Solution-

6752 | *Catal. Sci. Technol.*, 2025, **15**, 6744–6756

This journal is © The Royal Society of Chemistry 2025

phase ^{1}H, ^{13}C and ^{19}F NMR spectra of **1–11** were recorded on a Bruker AVANCE III 400 MHz spectrometer using MestReNova software. The solid-state ^{19}F MAS-NMR spectra of F–TiO$_2$ NPs were recorded on a Bruker AVANCE III 500 WB spectrometer in a 2.5 mm triple $H/X/Y$ probe with an applied rotation frequency of 18–28–30 kHz. TGA data of molecular precursors were collected at atmospheric pressure under an inert gas flow of 30 mL min^{-1} of argon or 20 mL min^{-1} of nitrogen using a Setaram TGA92-12 thermal analyzer (with a thermal ramp of 5 °C min^{-1}). Powder XRD diffraction experiments were carried out with a Bruker D8 Advance A25 system with Cu Kα_{1+2} (λ = 0.154184 nm) radiation. N$_2$ adsorption and desorption isotherms of the F–TiO$_2$ catalysts, pre-treated at 100 °C (with a heating rate of 5 °C min^{-1}) under vacuum for 24 h, were obtained with a Micrometric ASAP 2020 instrument at 77 K. The XPS characterization was performed on a Kratos Axis Ultra DLD spectrometer equipped with a hemispherical electron analyzer using monochromatic Al K-α X-ray radiation (1486.6 eV, 12 kV × 15 mA = 180 W). Survey spectra were recorded with a pass energy of 160 eV and 1 eV step. High resolution spectra were recorded with a 30 eV pass energy and 0.1 eV step in the F 1s, O 1s, C 1s and Ti 2p regions. The binding energy of the C 1s peak at 284.8 eV was taken as the internal standard. The CasaXPS software version 2.3.25 was used for data treatment. The XRF analysis was carried out with a wavelength dispersive X-ray fluorescence spectrometer, Malvern's Zetium PANalytical. Before analysis, samples were mixed with boric acid to obtain a 200 mg powder pellet (sample + boric acid) with a diameter of 13 mm.

Synthesis of new fluorinated Ti(ιν) precursors 1–11

The bis complexes **1–4** were prepared by reacting Ti(OEt)$_4$ or Ti(NMe$_2$)$_4$ with 2 equivalents of fluorinated aminoalkoxides F-dmapH or F-dmampH in toluene. After stirring the reaction mixture for 4 h at room temperature, the solvents were removed under vacuum to yield a colorless (for **1** and **3**) or yellowish-brown viscous oil (for **2** and **4**) at room temperature. Among these, only complex **3** could be crystallized from a concentrated *n*-hexane solution at low temperature. However, the low-melting nature of this complex prevented its characterization by single crystal X-ray structure analysis. These complexes **1–4**, which could not be distilled either under vacuum, reacted further with hexafluoroisopropanol (hfipH) at room temperature to afford heteroleptic precursors **5** and **6** with two different fluorinated ligands (hfip and F-dmap or F-dmamp). Complexes **7** and **8** with three different ligands (hfip, non-fluorinated mdea, and OEt or NMe$_2$) were synthesized by step-wise addition of the ligands. In view of the similarity of the synthesis of **1–8**, only one synthesis is described in detail below (for **8**).

[Ti$_2$(hfip)$_2$(mdea)$_2$(NMe$_2$)$_2$] (8)

In a Schlenk tube containing Ti(NMe$_2$)$_4$ (1 g, 4.4 mmol) and toluene (25 mL), *N*-methyl-diethanolamine (mdeaH$_2$) (0.5 g,

4.4 mmol) was added dropwise and the reaction mixture was stirred at room temperature for 1 h. Subsequent addition of 1 equivalent of hfipH (0.75 g, 4.4 mmol) and stirring the reaction mixture for 4 h yielded a homogeneous transparent solution, which was concentrated and kept at −5 °C to afford red plate-shaped crystals of the target product **8**. Yield: 1.9 g (85%).

The dinuclear oxo-complexes [Ti$_2$(μ-O)$_2$(η^2-OR$_F$)$_4$] [OR$_F$ = F-dmap (**9**) and F-dmamp (**10**)] were synthesized by the partial hydrolysis of precursors **1–4** in toluene, whereas the pentanuclear oxo cluster [Ti$_5$O$_3$(mdea)$_5$(hfip)$_4$] (**11**) was obtained by *in situ* hydrolysis during the reaction of Ti(OEt)$_4$ with mdeaH$_2$ and hfipH in *n*-pentane using a hydrolysis ratio of 0.1. After stirring for 4 h at room temperature, the reaction mixture was concentrated and kept at −5 °C to afford colorless crystals of **9–11**. Table S11 contains the yield and elemental analyses for products **1–11**, whereas their spectroscopic data are provided in Table S12.

Single crystal X-ray crystallography

Crystals structures of **5–11** were determined using an Xcalibur Gemini kappa-geometry diffractometer equipped with an Atlas CCD and a molybdenum X-ray source (l = 0.71073 Å). Intensities were collected by means of the CrysAlisPro software.[44] Reflection indexing, unit-cell parameter refinement, Lorentz-polarization correction, absorption correction, peak integration and background determination were carried out with the CrysAlisPro software.[44] The resulting set of *hkl* was used for structure solution and refinement. The structures were solved with the ShelXT[45] structure solution program using the intrinsic phasing solution method and by using Olex2 (ref. 46) as the graphical interface. The model was refined with version 2018/3 of ShelXL[45] using least-squares minimization.

Powder X-ray diffraction data

PXRD data were collected on a Bruker D8 advance diffractometer in a Bragg Brentano mode equipped with a Lynxeye detector and copper radiation (K$\alpha_{1,2}$ = 1.5418 Å). Rietveld refinement was applied on some selected F–TiO$_2$ NPs using the Fullprof_suite program.[47] An anisotropic size model was used to estimate the crystallite size.

Synthesis of F-doped TiO$_2$ NPs

The F-doped TiO$_2$ NPs were obtained by complete hydrolysis of the fluorinated Ti(ιν) precursors **1–11** in aqueous medium in the presence of 0.1 equivalent of NH$_4$F. The purified precursors were added to boiling deionized water and the reaction mixture was refluxed for 1 h. The white powders obtained after centrifugation were washed twice each with 20 mL of water and ethanol and finally dried at 70 °C for 12 h. For comparative studies, the undoped TiO$_2$ was also obtained by the hydrolysis of Ti(OEt)$_4$ in the presence of NBu$_4$Br.[29]

This journal is © The Royal Society of Chemistry 2025

Catal. Sci. Technol., 2025, **15**, 6744–6756 | 6753

Measurements of acidic properties

FTIR of pyridine-adsorption. FT-IR of adsorbed pyridine was carried out to probe the nature of the acid sites. Catalyst powders were pressed into self-supported pellets (50 mg of catalyst, 18 mm diameter). The pellets were placed in an IR Pyrex cell equipped with KBr windows. First, pellets were vacuum treated at 200 °C for 1 h (TiO_2 and $F–TiO_2$), and then exposed to pyridine vapor pressure at room temperature for 30 min. The desorption was performed by outgassing the samples for 1 h at RT and 200 °C and the FT-IR spectra of adsorbed pyridine were recorded at room temperature after each step. Lewis and Brønsted acidity quantifications were done by integrating the FTIR spectra after Py-desorption at 200 °C using OPUS software, where two bands at 1446 and 1541 cm^{-1} were selected for the Lewis and Brønsted acid sites, respectively.

Calorimetry (NH_3 adsorption). Calorimetry was performed to study the original acid-properties of the solid. The experimental set up consists of a TainCalvet calorimeter connected to vacuum glass volumetric equipment to measure the differential heat of adsorption of the successive small amount of the probe molecule up to the surface coverage and, in parallel, the isotherm of NH_3 adsorption. About 50 mg of sample was placed in a glass cell and further treated under vacuum at 150 °C for 4 h, and then placed into the calorimeter and kept under vacuum overnight. Small doses of ammonia were introduced into the glass cell till the equilibrium pressure of the probe molecule was reached. The NH_3 adsorption was performed at 80 °C.

Measurements of catalytic properties

Gas phase isopropanol conversion reaction. The isopropanol dehydration reaction was used to evaluate the acidity of the catalyst. 80 mg of the catalyst was placed inside a continuous flow reactor and heated *in situ* at a rate of 5 °C min^{-1} and up to 200 °C for 1 h. 8.7 Torr isopropanol diluted in N_2 was allowed to pass through the catalyst at the same temperature with a flow of 5 L h^{-1} (N_2 flow previously passed through a saturator filled with isopropanol and kept at 70 °C). The products obtained were analyzed by gas chromatography using a Shimadzu GC-2030 gas chromatograph with an FID and helium as a gas vector. The column used was a CP-PoraBond Q (25 m, 0.53 mm, 10 μm) and the injector temperature was 250 °C. The GC also contained a TCD with helium as a gas vector; the column was a CarboPlot P7 (25 m, 0.53 mm, 25 μm). The maximum temperature was 115 °C. The turnover frequency value (TOF) was calculated as a relation of the number of moles of IPA converted per acid site mole in a unit of time.

Aqueous phase dihydroxyacetone (DHA) conversion. DHA conversion reactions were performed using a batch reactor equipped with a controlling instrument for the temperature, pressure and stirring (Fig. S19). 25 mg of the catalyst was placed inside the reactor cell followed by the addition of 25 mg of DHA (powder Aldrich) and 50 ml of deionized water. The cell was then placed inside the reactor, and the tightly closed reactor was allowed to have an argon pressure of 6 bar. The stirring was set at 300 rpm. The reactant/product analysis was done using high-performance liquid chromatography (HPLC) (Model Shimadzu Prominence) with a refractive index detector (RID) equipped with a COROGEL 107H column, at 40 °C, and acidified water (H_2SO_4 2.5 mM) was used as a mobile phase (0.6 mL min^{-1}).

Author contributions

Fouad Elgayar: writing – original draft, investigation. Erwann Jeanneau: formal analysis, data curation (single crystal XRD). Pascal Bargiela: formal analysis (XPS). Adel Mesbah: validation, formal analysis (powder XRD), supervision, project administration. Nadine Essayem: writing – review & editing, validation, supervision, resources, project administration, funding acquisition, conceptualization. Shashank Mishra: writing – review & editing, writing – original draft, validation, supervision, resources, project administration, methodology, funding acquisition, conceptualization.

Conflicts of interest

There are no conflicts to declare.

Data availability

Supplementary information: FT-IR, ^1H, ^{13}C and ^{19}F NMR, single crystal X-ray diffraction and TGA data of the precursors, XRD, ^{19}F MAS-NMR, XPS spectra, Kubelka–Munk plots, contact angle measurements of $F-TiO_2$ and TiO_2 catalysts, and mechanisms of IPA and DHA conversion). See DOI: **https://doi.org/10.1039/D5CY00688K**.

CCDC 2425366–2425371, 2427765 and 2427766 contain the supplementary crystallographic data for this paper.[48a–h]

Data will be made available on request.

Acknowledgements

References

1 (a) X. Wu, X. Fan, S. Xie, J. Lin, J. Cheng, Q. Zhang, L. Chen and Y. Wang, *Nat. Catal.*, 2018, **1**, 772–780; (b) M. J. Hülsey, H. Yang and N. Yan, *ACS Sustainable Chem. Eng.*, 2018, **6**, 5694–5707.

2 (a) W. Leitner, J. Klankermayer, S. Pischinger, H. Pitsch and K. Kohse-Höinghaus, *Angew. Chem., Int. Ed.*, 2017, **56**, 5412–5452; (b) M. Raud, T. Kikas, O. Sippula and N. J. Shurpali, *Renewable Sustainable Energy Rev.*, 2019, **111**, 44–56.

6754 | *Catal. Sci. Technol.*, 2025, **15**, 6744–6756

This journal is © The Royal Society of Chemistry 2025

3 Y. Guo, M. Fang, S. Yuan, Z. Yang and X. Xia, *Chem. Eng. Sci.*, 2024, **299**, 120555.

4 (*a*) A. Bohre, S. Dutta, B. Saha and M. Abu-Omar, *ACS Sustainable Chem. Eng.*, 2015, **2**, 1263–1277; (*b*) Y. Lou and D. F. Shantz, *ChemCatChem*, 2019, **11**, 1328–1336.

5 G. Li, N. Li, Z. Wang, C. Li, A. Wang, X. Wang, Y. Cong and T. Ahang, *ChemSusChem*, 2012, **5**, 1958–1966.

6 C. Wen, E. Barrow, J. Hattrick-Simpers and J. Lauterbach, *Phys. Chem. Chem. Phys.*, 2014, **16**, 3047.

7 A. Samikannu, L. J. Konwar, K. Rajendran, C. C. Lee, A. Shchukarev, P. Virtanen and J.-P. Mikkola, *Appl. Catal., B*, 2020, **272**, 118987.

8 R. Cai, X. Pei, H. Pan, K. Wan, H. Chen, Z. Zhang and Y. Zhang, *Energy Fuels*, 2020, **34**, 11771–11790.

9 M. Kapilashrami, Y. Zhang, Y.-S. Liu, A. Hagfeldt and J. Guo, *Chem. Rev.*, 2014, **114**, 9662–9707.

10 P. Sudarsanam, H. Li and T. V. Sagar, *ACS Catal.*, 2020, **10**, 9555–9584.

11 R. B. Salem, M. Eternot, B. Purohit, P. Bargiela, N. Essayem and S. Mishra, *ChemCatChem*, 2025, **17**, e202401530.

12 A. B. S. Neto, A. C. Oliveira, S. Mishra and N. Essayem, *Appl. Catal., A*, 2023, **658**, 119165.

13 S. Celerier and F. Richard, *Catal. Commun.*, 2015, **67**, 26.

14 E. Kemnitz, *Catal. Sci. Technol.*, 2015, **5**, 786.

15 S. Liu, J. Yu, B. Cheng and M. Jaroniec, *Adv. Colloid Interface Sci.*, 2012, **173**, 35–53.

16 A. Corma and V. Fornes, *Appl. Catal.*, 1990, **61**, 175.

17 (*a*) E. M. Samsudin, S. B. A. Hamid, J. C. Juan, W. J. Basirun, A. E. Kandjani and S. K. Bhargava, *Appl. Surf. Sci.*, 2016, **365**, 57–68; (*b*) J. C. Yu, N. Yu, N. Ho, N. Jiang and N. Zhang, *Chem. Mater.*, 2002, **14**, 3808–3816.

18 S.-M. Wu and P. Schmuki, *Energy Technol.*, 2023, **11**, 2300052.

19 S. Mishra and S. Daniele, *Chem. Rev.*, 2015, **115**, 8379–8448.

20 A. Verchère, S. Mishra, E. Jeanneau, H. Guillon, J.-M. Decams and S. Daniele, *Inorg. Chem.*, 2020, **59**, 7167–7180.

21 S. Mishra and S. Daniele, *Chem. – Eur. J.*, 2020, **26**, 9292–9303.

22 A. B. S. Neto, M. G. A. Cruz, E. Jeanneau, A. C. Oliveira, N. Essayem and S. Mishra, *Dalton Trans.*, 2021, **50**, 1604–1609.

23 S. Mishra, E. Jeanneau, M. Rolland and S. Daniele, *RSC Adv.*, 2016, **6**, 1738–1743.

24 S. Mishra, V. Mendez, E. Jeanneau, V. Caps and S. Daniele, *Eur. J. Inorg. Chem.*, 2013, 500–510.

25 S. Mishra, E. Jeanneau, S. Daniele and V. Mendez, *Dalton Trans.*, 2010, **39**, 7440–7443.

26 S. Mishra, S. Daniele, S. Petit, E. Jeanneau and M. Rolland, *Dalton Trans.*, 2009, 2569–2577.

27 T. Kemmitt, N. I. Al-Salim, G. J. Gainsford and W. Henderson, *Aust. J. Chem.*, 1999, **52**, 915.

28 M. North, *Principles and Applications of Stereochemistry*, CRC Press, Cheltenham, 1998.

29 G. Goutailler, C. Guillard, S. Daniele and L. G. Hubert-Pfalzgraf, *J. Mater. Chem.*, 2002, **13**, 342–346.

30 J. C. Yu, H. Yu and Z. Jiang, *Chem. Mater.*, 2002, **14**, 3808–3816.

31 L. Ruan, X. Wang, T. Wang, Z. Ren, Y. Chen, R. Zhao, D. Zhou, G. Fu, S. Li, L. Gao, Y. Lu, Z. Wang, H. Tian, X. Kong and G. Han, *ACS Appl. Mater. Interfaces*, 2019, **11**, 37256–37262.

32 (*a*) T. Koketsu, *et al.*, *Nat. Mater.*, 2017, **16**, 1142–1148; (*b*) S.-M. Wu, *et al.*, *ACS Catal.*, 2023, **13**, 33–41.

33 R. B. Salem, T. Cornier, P. Bargiela, B. Lebeau, S. Mishra and N. Essayem, *ChemCatChem*, 2023, **15**, e202300169.

34 S. Gahlot, E. Jeanneau, F. Dappozze, C. Guillard and S. Mishra, *Dalton Trans.*, 2018, **47**, 8897–8905.

35 J. C. Yu, W. Ho, J. Yu, S. K. Hark and K. Iu, *Langmuir*, 2003, **19**, 3889–3896.

36 J. Yu, W. Wang, B. Cheng and B.-L. Su, *J. Phys. Chem. C*, 2009, **113**, 6743–6750.

37 M. A. Bhide, K. L. Mears, C. J. Carmalt and C. E. Knapp, *Chem. Sci.*, 2021, **12**, 8822–8831.

38 J. Yu, J. C. Yu, M. K.-P. Leung, W. Ho, B. Cheng, X. Zhao and J. Zhao, *J. Catal.*, 2003, **217**, 69–78.

39 D. Bersani, P. P. Lottici and X.-Z. Ding, *Appl. Phys. Lett.*, 1998, **72**, 73–75.

40 I. Abdouli, F. Dappozze, M. Eternot, C. Guillard and N. Essayem, *Molecules*, 2022, **27**, 8172.

41 A. Gervasini, J. Fenyvesi and A. Auroux, *Catal. Lett.*, 1997, **43**, 219–228.

42 J. Dijkmans, M. Dusselier, D. Gabriëls, K. Houthoofd, P. C. M. M. Magusin, S. Huang, Y. Pontikes, M. Trekels, A. Vantomme, L. Giebeler, S. Oswald and B. F. Sels, *ACS Catal.*, 2014, **5**, 928–940.

43 H. Zhu, X. Xu, Y. Wang, J. Ding, X. Yu, X. Liu, Z. Zeng, H. Wang, Z. Li and Y. Wang, *Nanoscale*, 2024, **16**, 12992–12999.

44 *CrysAlisPro Software system, Rigaku Oxford Diffraction*, version 1.171.43.105a, 2024.

45 G. M. Sheldrick, *Acta Crystallogr., Sect. C:Struct. Chem.*, 2015, **71**, 3–8.

46 O. V. Dolomanov, L. J. Bourhis, R. J. Gildea, J. A. K. Howard and H. J. Puschmann, *Appl. Crystallogr.*, 2009, **42**, 339–341.

47 C. Frontera and J. Rodríguez-Carvajal, *Phys. B*, 2003, **335**, 219–222.

48 (*a*) F. Elgayar, E. Jeanneau, P. Bargiela, A. Mesbah, N. Essayem and S. Mishra, CCDC 2425366: Experimental Crystal Structure Determination, 2025, DOI: **10.5517/ccdc.csd.cc2mdsmg**; (*b*) F. Elgayar, E. Jeanneau, P. Bargiela, A. Mesbah, N. Essayem and S. Mishra, CCDC 2425367: Experimental Crystal Structure Determination, 2025, DOI: **10.5517/ccdc.csd.cc2mdsnh**; (*c*) F. Elgayar, E. Jeanneau, P. Bargiela, A. Mesbah, N. Essayem and S. Mishra, CCDC 2425368: Experimental Crystal Structure Determination, 2025, DOI: **10.5517/ccdc.csd.cc2mdspj**; (*d*) F. Elgayar, E. Jeanneau, P. Bargiela, A. Mesbah, N. Essayem and S. Mishra, CCDC 2425369: Experimental Crystal Structure Determination, 2025, DOI: **10.5517/ccdc.csd.cc2mdsqk**; (*e*) F. Elgayar, E. Jeanneau, P. Bargiela, A. Mesbah, N. Essayem and S. Mishra, CCDC 2425370: Experimental Crystal Structure Determination, 2025, DOI: **10.5517/ccdc.csd.cc2mdsrl**; (*f*) F. Elgayar, E. Jeanneau, P. Bargiela, A. Mesbah, N. Essayem and S. Mishra, CCDC 2425371: Experimental Crystal Structure Determination, 2025, DOI:

This journal is © The Royal Society of Chemistry 2025

Catal. Sci. Technol., 2025, **15**, 6744–6756 | **6755**

10.5517/ccdc.csd.cc2mdssm; (*g*) F. Elgayar, E. Jeanneau, P. Bargiela, A. Mesbah, N. Essayem and S. Mishra, CCDC 2427765: Experimental Crystal Structure Determination, 2025, DOI: 10.5517/ccdc.csd.cc2mh90g; (*h*)

F. Elgayar, E. Jeanneau, P. Bargiela, A. Mesbah, N. Essayem and S. Mishra, CCDC 2427766: Experimental Crystal Structure Determination, 2025, DOI: 10.5517/ccdc.csd.cc2mh91h.

6756 | *Catal. Sci. Technol.*, 2025, **15**, 6744–6756

This journal is © The Royal Society of Chemistry 2025